npj | 2D materials and applications

www.nature.com/npj2dmaterials

ARTICLE OPEN

Check for updates

Mechanistic insights into the deformation and degradation of a 2D metal organic framework

Hafeesudeen Sahabudeen[1], Qiang Zhang[1], Yue Liu[1], Matthias Heuchel[1] and Rainhard Machatschek[1]✉

2D metal-organic frameworks (2D-MOFs) materials can be subjected to various modes of mechanical stresses and strains in a wide range of applications, for which their mechanical properties are critical to reach practical implementations. Despite the rapid developments focused on the preparation of ultrathin 2D-MOF materials, very little is known about their mechanical and degradation behavior. Here, we use the established 2D-MOF PdTCPP-Cu (NAFS-13) as model system, to introduce the Langmuir–Blodgett (LB) technique, combined with interfacial rheology, as a novel in situ method for direct determination of the in-plane Young's modulus by simultaneously measuring the 2D shear and compression moduli of a 2D-MOF formed at the air-water interface. Furthermore, it can be used to evaluate mechanistic models describing the degradation kinetics of 2D MOFs. To provide a deeper understanding of the factors that determine the Young's modulus observed in such a set up, we carried out nanoindentation measurements and molecular dynamics (MD) simulations based on classical force fields. This protocol allows us to gain mechanistic insights into the impact of structural defects, temperature, tensile and compression stress on the Young's modulus of 2D MOFs.

npj 2D Materials and Applications (2023)7:25 ; https://doi.org/10.1038/s41699-023-00391-3

INTRODUCTION

Understanding the underlying mechanisms determining the mechanics of 2D materials offers exciting opportunities for designing materials towards a wide range of applications, including flexible electronics[1], strain sensors[2,3], nanogenerators[4], innovative nanoelectromechanical systems (NEMS)[5] and biomedicine[6]. In particular, the development of flexible devices requires a thorough knowledge about the mechanics of the applied 2D materials. For instance, 2D materials (e.g. Graphene, MoS_2, WS_2, etc.) with atomic thickness and ultrahigh flexibility are suitable for conducting and transparent electrodes in flexible and foldable electronics[1] where their Young's modulus and fracture behaviors are of vital importance[7]. Compared to inorganic 2D materials, organometallic materials such as 2D metal-organic frameworks (2D-MOFs) are generally softer and more flexible and exhibit diverse functionalities originating from versatile structures, highly accessible active sites, tailorable chemical compositions, and many unique physicochemical properties[8]. Given the recent progress in the preparation of 2D-MOFs, it is remarkable how little is known about their mechanical behavior. Clearly, the structural flexibility or stiffness (Young's modulus) and film-to-substrate adhesion are key aspects when considering practical applications such as chemo-switching or sensing applications[9], catalytic devices[10], membranes and actuators[11]. For example, in stress-induced chemical sensing devices based on thin MOF films integrated with microcantilevers, the film stiffness (i.e. Young's modulus) and the film-to-substrate adhesion strength are key mechanical properties controlling plastic deformation and shear delamination failures[9]. In addition, the performance of piezoelectric devices such as actuators is strongly dependent on the elastic properties of the MOF structure to enhance the effective electro-mechanical energy conversion[12]. Moreover, since all building blocks of a 2D-MOF are permanently exposed to the environment, these materials are especially at risk of undergoing chemical changes, which can cause bond cleavage and degradation. Understanding how this affects the mechanics of these materials is indispensable to predict their long-term performance in any of the aforementioned applications.

MOFs are typically obtained as insoluble and un-processable powders by conventional synthetic techniques such as solvothermal/hydrothermal methods[13]. Therefore, controlling the sheet size and dimensionality resulting from the exfoliation process remains an important challenge. Moreover, utilizing 2D MOFs in nanotechnological devices such as sensors and membranes requires their fabrication into films. Here, the Langmuir–Blodgett (LB) technique represents a promising bottom-up approach to create large-area, tightly packed arrays of 2D MOF sheets on liquid surfaces that can be deposited and stacked onto solid substrates[14–17]. While it can be used to control the assembly of preformed 2D sheets[18], it is very advantageous to form the sheets directly at the interface, where the low surface roughness of water (~ 3 Å) ensures that the growth reaction will be in-plane[19]. Moreover, the interface imparts an orientation onto anchoring molecules while allowing for mobility to enable an efficient assembly[20] and reassembly. It is expected that these 2D films, due to their high structural flexibility[21] and the presence of water, respond differently to external stimuli than a structurally analogous bulk material or a thin film in the dry state. Therefore, Langmuir films are especially valuable for characterizing the mechanical behavior of 2D MOFs with applications in aqueous environments, but so far, no method for in situ characterization of the mechanics of 2D-MOF nanosheets at the air-water interface has been proposed. The current experimental methods to investigate the mechanical properties of monolayer 2D MOFs include atomic force microscopy-based nanoindentation[22–24] and buckling-based metrology[25]. The quantification of mechanical properties of ultrathin MOFs by these approaches remains challenging, as it always involves the transfer of nanosheets onto solid substrates, which can cause structural distortion (i.e. folding/tearing of sheets). The nanoindentation tests apply tensile stress

[1]Institute of Active Polymers, Helmholtz-Zentrum Hereon, Kantstraße 55, 14513 Teltow, Germany. ✉email: rainhard.machatschek@hereon.de

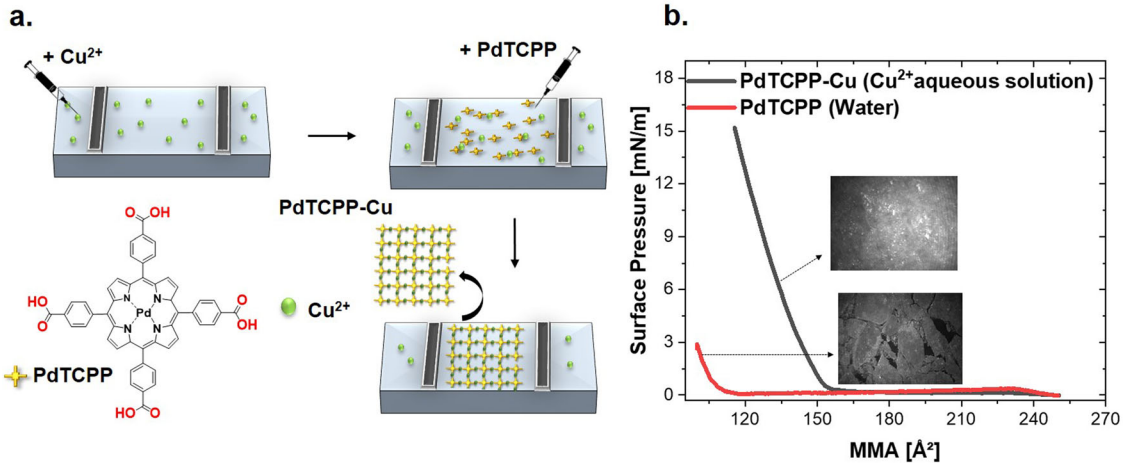

Fig. 1 Synthesis of 2D MOF at the Air – Water interface. a Schematic illustration of the representative assembly processes of PdTCPP-Cu at the air-water interface. The PdTCPP-Cu monolayer was prepared in a Langmuir trough by spreading the PdTCPP molecules onto an aqueous solution of Cu^{2+} metal ions. **b** Surface pressure (π) versus mean molecular area (MMA) isotherm curves for PdTCPP monolayers in Cu^{2+} aqueous solution (black line) and pure water (red line) as sub-phases. Inset shows the Brewster angle microscopy images of a packed monolayer of PdTCPP-Cu in Cu^{2+} aqueous solution and assembly of PdTCPP monomer on the pure water subphase.

and do not provide information on compression behavior and associated mechanical properties of 2D materials. Moreover, nanoindentation can deform only a small area under the indenter tip and does not provide a reliable assessment of the mechanical performance of a large-area sheet relevant for practical applications[26,27]. Therefore, the development of a complementary in-situ methodology is highly essential. Here, we hypothesize that the LB technique, when combined with interfacial rheology, enables the direct measurement of the in-plane Young's modulus of 2D materials in contact with an aqueous environment, thereby eliminating any artifacts arising from film transfer or substrate interactions. Furthermore, this methodology provides an elegant route to analyze the degradation behavior of 2D MOFs in real time, and to establish a mechanistic model describing their loss of strength and mass over time, which are highly relevant for several biomedical applications.

In this work, a 2D MOF based on PdTCPP and Cu^{2+} moieties was used as a model system, for which the formation mechanism and the corresponding structural characterization are well documented in the literature[17,28]. To this end, the 2D shear modulus *G* and compression modulus *K* of a 2D MOF formed at the air-water interface were measured simultaneously and the Young's modulus *E* was calculated according to the relation of the elastic moduli[29,30]. The 2D compression modulus of the PdTCPP-Cu monolayer was obtained by measuring the surface pressure π vs. mean molecular area (MMA) isotherm as the monolayer was compressed to a preset surface pressure. Simultaneously, the interfacial shear modulus was measured using a biconical disk rheometer positioned in the interface. Utilizing the same experimental setup, the degradation mechanism was further investigated by lowering the pH of the subphase below the PdTCPP-Cu monolayer, both at constant surface pressure (isobaric degradation) and constant surface area (isochoric degradation). The experimental data could be fitted with a simple analytical model based on a spring network where springs are cut randomly following first order kinetics. To validate the experimental results and to better understand which parameters influence the Young's modulus measured by the LB technique and by nanoindentation, an atomistic model of the 2D MOF was developed. Molecular dynamics (MD) simulations of this model allowed to predict Young's moduli under tensile and compressive stresses while varying defect density, moisture and temperature.

RESULTS AND DISCUSSION

Synthesis of 2D MOF at the air – water interface

Copper mediated 2D MOF sheets (PdTCPP-Cu) were synthesized through a coordination reaction between the metalloporphyrin, 5,10,15,20-tetrakis (4- carboxyphenyl)-porphyrinato-palladium(II) (PdTCPP) and Copper(II) nitrate ($Cu(NO_3)_2$) at the air-water interface by the Langmuir-Blodgett technique. Our fabrication procedure to synthesize a large-area PdTCPP-Cu monolayer follows the previously published route[17] to prepare NAFS-13 (*na*nofilm of metal-organic *f*rameworks on *s*urfaces no. *13*) and is illustrated in Fig. 1a. The experiments were started with the spreading of a solution of carboxylic acid ligand (PdTCPP) in chloroform/methanol onto an aqueous solution of Cu^{2+} metal ions at the air/water interface. Compressing the molecules on the surface led to the formation of the densely packed monolayer of PdTCPP-Cu mediated by copper ions. A surface pressure vs. mean molecular area (MMA) isotherm was measured to further monitor the formation and packing orientation of PdTCPP molecules. As illustrated in the π-MMA isotherm (Fig. 1b), the large mean molecular area observed for the increase of π for the PdTCPP-Cu film demonstrates the linking of PdTCPP molecules via copper ion joints. The resulting arrays lie flat on the air-water interface. In the absence of Cu^{2+} ions (pure water subphase), the smaller MMA for the onset of an increase of π implies a different packing arrangement, with the PdTCPP molecules packing more closely with the porphyrin plane perpendicular to the water surface. The observed surface π-MMA isotherm of the PdTCPP-Cu sheet is in good agreement with those reported for CoTCPP-py-Cu (NAFS-1)[31] and H_2TCPP-Cu (NAFS-2)[28] analogues providing evidence that the linking of PdTCPP molecules occurs via copper ion joints and the resulting arrays lie flat on the air/water interface [17]. The formation of a cohesive film was further confirmed by a series of Brewster-angle microscopy (BAM) images recorded at different surface pressures of PdTCPP (water subphase) and PdTCPP-Cu (Cu^{2+} aqueous solution as subphase) (Fig. 1b). A homogeneous monolayer of PdTCPP-Cu was observed on the Cu^{2+} aqueous solution, whereas several defects were observed for PdTCPP in the pure water subphase.

The synthesized PdTCPP-Cu sheet could be readily transferred to Si/SiO_2 substrates for further characterization. Optical microscopy of transferred films showed thin homogeneous layers over areas of several mm^2 without any wrinkles. Some cracks were

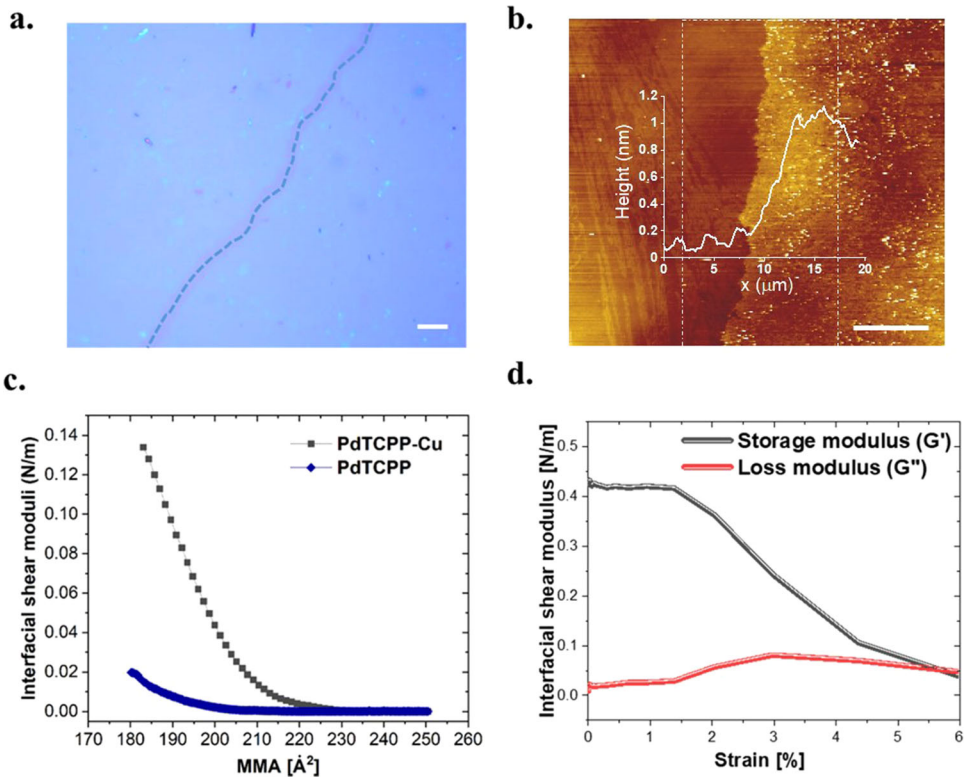

Fig. 2 Morhphology and rheology of the 2D MOF. a Optical microscopy image of monolayer PdTCPP-Cu deposited on Si with 300 nm SiO_2 (scale bar = 10 μm). The dashed line indicates the centerline of scratch created to visualize the layer. **b** AFM image of the PdTCPP-Cu on Si covered with 300 nm SiO_2 (inset: averaged height profiles along the scratch of the area circled with dashed line), scale bar = 10 μm. **c** Interfacial shear storage modulus of PdTCPP and PdTCPP-Cu film at the air-water interface at a frequency of 1 Hz and Strain of 1%, PdTCPP monolayers in Cu^{2+} aqueous solution (black) and pure water (blue) as subphases. **d** Variation in interfacial shear moduli with strain amplitude sweep at the frequency of 1 Hz. Interfacial storage (black line) and loss modulus (red line) of PdTCPP-Cu film.

observed, which are likely due to the mechanical strain caused during the transfer or/and drying process (Fig. 2a). The scratch in the PdTCPP-Cu monolayer sheet shown in Fig. 2a was created manually to enhance the contrast and to distinguish between the covered area and bare substrate surface. The corresponding atomic force microscopy (AFM) height image and the cross-sectional analysis along the edges indicate that the PdTCPP-Cu layer has a thickness of 0.9 ± 0.08 nm, thus suggesting the single layer feature of the PdTCPP-Cu 2D-MOF (Fig. 2b).

In-situ interfacial rheology

The formation of the cohesive film was further confirmed by interfacial rheology. The presence of a storage shear modulus implies that the monolayer assembles as a two-dimensional solid rather than a network of independent particles[32,33]. As shown in Fig. 2c, the interlinking of Cu^{2+} ion with PdTCPP enhances the maximum shear modulus (0.14 N m^{-1}) when compared to the PdTCPP molecules (0.02 N m^{-1}) in water. The storage and elastic moduli of the PdTCPP-Cu 2D-MOF single layer is stable in the long term shear measurement (Supplementary Fig. 1b). However, in the absence of Cu^{2+} ions, the shear modulus of PdTCPP films decreased drastically with time, indicating no 2D framework was formed (Supplementary Fig. 1a). A magnified view (Fig. 3b) shows that the interfacial shear modulus increases strongly at an MMA of about 230 $Å^2$. The area of the unit cell of PdTCPP-Cu is 275 $Å^2$, suggesting that the average layer thickness is about 20% greater than the ideal monolayer value when the film becomes cohesive, which supports that the film is of predominantly monolayer thickness. Furthermore, the viscoelastic behavior of the PdTCPP-Cu monolayer was measured by the amplitude sweep test at a frequency of 1 Hz (Fig. 2d). The linear viscoelastic region of PdTCPP-Cu is identified as the range within which the modulus is not affected by the applied shear strain. Increasing the strain up to a critical amplitude value will initiate disturbances within the framework, resulting in a decrease of the storage modulus (G'). Here, G' of PdTCPP-Cu remained constant in the strain range of 0.01-1.4%, indicating that the 2D MOF layer was not irreversibly deformed. The transition point at the deviation region from the linear to non-linear viscoelastic behavior is defined as the critical strain value (ϵ_c)[34]. In this study, the critical strain value is around 1.4%, where G' starts to drop. The PdTCPP-Cu film is elastic up to the strain of 1.4%, at which the storage modulus decrease and the loss modulus (G'') increases in the amplitude sweep.

The Young's modulus of any material can be calculated from the compression modulus (K) and the shear modulus (G). The latter can be obtained from the in-situ interfacial rheological experiment (Fig. 3b), whereas K is calculated from the surface pressure vs. area isotherm[32,35]

$$K = -A_{MMA}\frac{d\pi}{dA_{MMA}} \quad (1)$$

The 2D compression modulus of the PdTCPP-Cu monolayer was obtained by measuring the π vs. MMA isotherm as the monolayer is compressed to a preset pressure of $\pi = 5$ mN m^{-1} (Fig. 3a). During the compression process, the molecules in the monolayer are approaching, and the interactions between them are getting stronger leading to the formation of a condensed monolayer as evident by the increase in K.

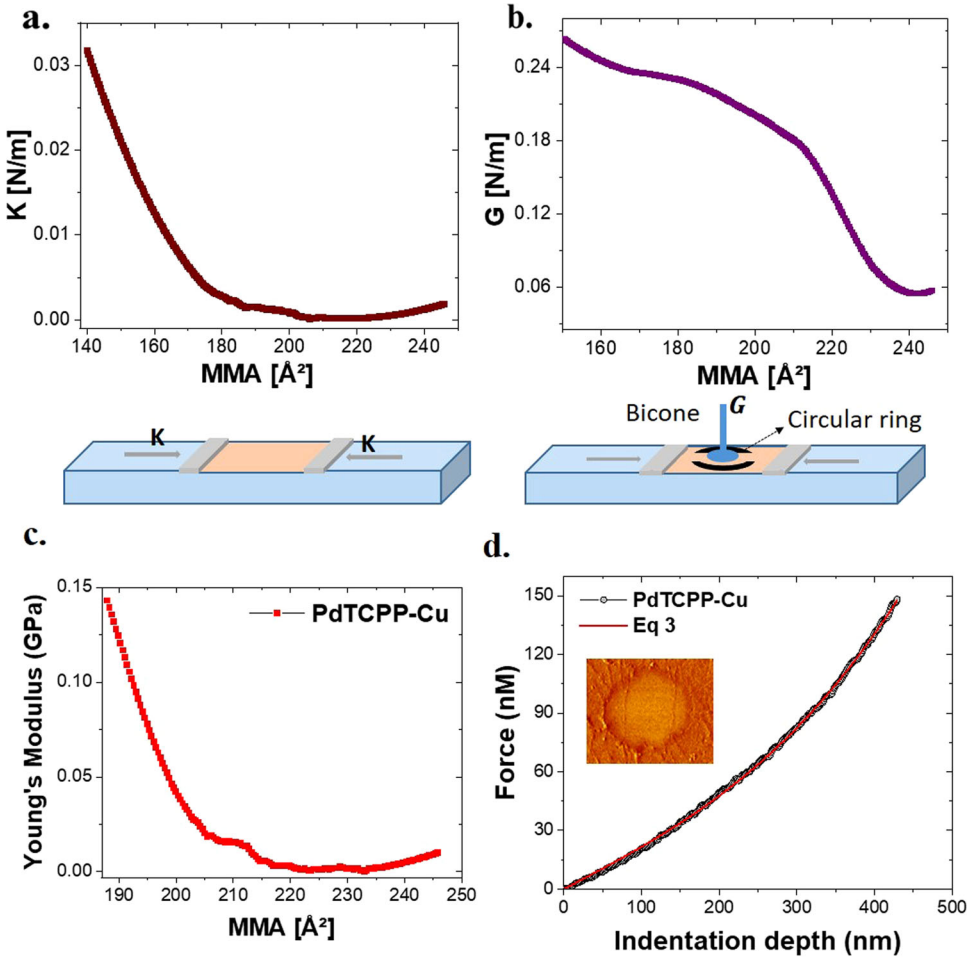

Fig. 3 Mechanical moduli determined by the Langmuir technique and nano-indentation. a The 2D compression modulus of the PdTCPP-Cu monolayer was obtained by measuring the π-MMA isotherm as the monolayer is compressed to a preset pressure. **b** The interfacial shear storage modulus *G'* was measured using a biconical disk rheometer positioned in the interface. **c** The Young's modulus of the PdTCPP-Cu monolayer was calculated from *G* and *K*. **d** AFM nanoindentation-based loading/unloading force curve measured at the center of the freestanding 2D MOF sheet as shown in the inset and curve fitting to Eq. (3).

The Young's modulus (*E*) of the PdTCPP-Cu monolayer (Fig. 3c) is calculated from *G* and *K* using the mathematical expression connecting the three moduli, which, in 2D, is given by[29,30]

$$E = \frac{4KG}{K+G} \tag{2}$$

Both the compressive and shear moduli attained their maximal values near the end of the monolayer regime, which should correspond to the stiffness of a PdTCPP-Cu film. The obtained Young's modulus *E* is on the order of ~ 0.18 GPa. Further compression of the film past the monolayer regime results in the formation of wrinkling patterns, which corresponds to a decrease in the slope of the isotherm as shown in Supplementary Fig. 2.

AFM nanoindentaion

To compare macroscopic compression behavior of the 2D MOF monolayer at the air-water interface with the nanoscopic tensile properties probed by AFM nanoindentation, suspended films were prepared by horizontally transferring the PdTCPP-Cu from the air-water interface onto the TEM grids with a circular mesh of diameter ~7 μm (Supplementary Fig. 3a and b). The areas marked with (I) in Supplementary Fig. 3b show the hole fully covered by PdTCPP-Cu in which the indentation experiment was performed, whereas area (II) features an empty hole without attached film. Mechanical characterization of the suspended flakes was probed by indenting the center of each film with an AFM tip. Mechanical testing was performed at a constant displacement rate, followed by load reversal. Upon the application of a load, the sheet was deformed (Fig. 3d). This deformation was quantified by recording the indentation depth at the sheet center as a function of the applied load. This cycle was repeated several times for each film tested. No evidence of the sheet sliding over the circular hole during the measurement was observed. The Young's modulus of the PdTCPP-Cu was determined by analyzing the individual loading/unloading force curves using the Eq. (3)[23,32]

$$F(\delta) = \pi T\delta + \frac{Ehq^3}{a^2}\delta^3 \tag{3}$$

where *F* is the loading force, *δ* is the indentation depth at the central point, *T* is the pretension accumulated in the sheet, *h* is the layer thickness, *a* is the membrane radius (~3.5 μm), $q = 1$ is a dimensionless constant. Fitting Eq. (3) to force-indentation curves yielded values of *E* ~ 12 GPa. The Young's modulus of PdTCPP-Cu obtained from AFM nanoindentation is comparable to bis(terpyridine)-metal complex nanosheet (16 GPa)[22] and covalently linked biphenyl sheets (~12 GPa)[36]. Clearly, Young's modulus of PdTCPP-Cu obtained from AFM nanoindentation is substantially higher than the value obtained from the in situ approach. To assess the reason behind this discrepancy, we carried out MD simulations of the 2D-MOF under different deformation conditions.

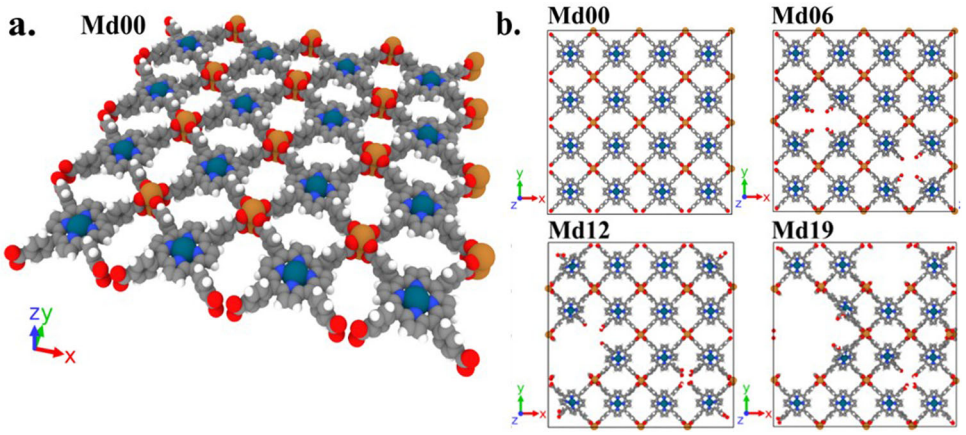

Fig. 4 Atomistic models for PdTCPP-Cu monolayer with and without defects. a Atomistic model Md00 for the defect free layer in 3D view. **b** Top view of four models with different defect percentage: Md00 with 0%, Md06 with 6.25%, Md12 with 12.50%, Md19 with 18.75%.

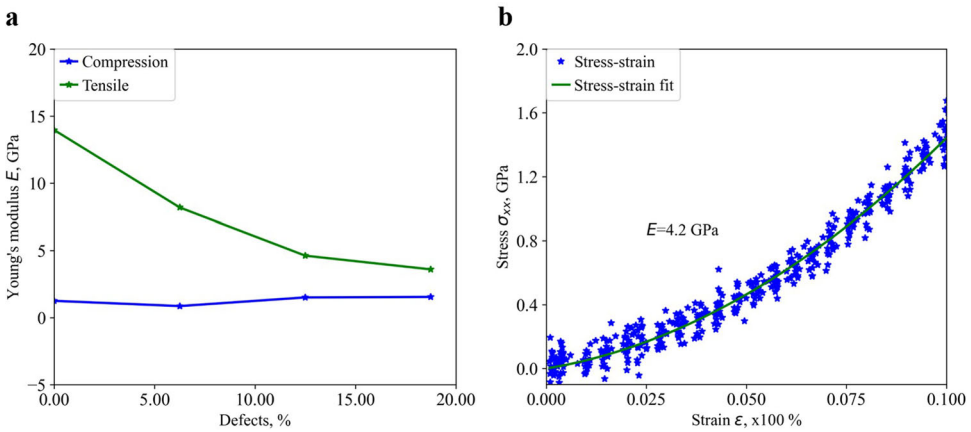

Fig. 5 Influence of defects and water on Young's modulus in MD simulations. a Calculated Young's moduli at various percentages of vacancy defects at 1 K and in vacuum using models Md00 till Md19. **b** Stress-strain curve of defect free PdTCPP-Cu (model Md00) on top of a water layer obtained at T = 300 K with maximum 10% uniaxial tensile strain. The data were fitted with Eq. (13) to extract the Young's modulus.

MD simulations of 2D MOF under uniaxial compression and tensile stress

Figure 4 shows the atomistic model for the PdTCPP-Cu 2D-MOF, consisting of a periodic supercell of a 4 ×4 square lattice structure. The atomistic model with no defects (Md00) has 1392 atoms. Further models were created with point defect contents of 6.25% (Md06), 12.50% (Md12) and 18.75% (Md19). The MD simulations were performed with the LAMMPS using UFF4MOF force field (see Methods). To calculate the Young's moduli, uniaxial tensile and compression runs in x and y directions were performed in NPT ensemble using Nose-Hoover thermostat and barostat.

The compression of an atomistic model of a PdTCPP-Cu monolayer to very low strains below 1% gave essentially the same Young's modulus as tensile deformation. Larger compressive strain caused a bending of the sheet, resulting in a situation that is very different from the flat 2D geometry observed during the tensile deformation (Supplementary Fig. 4). The corresponding potential energy as a function of strain for PdTCPP-Cu structures is summarized in Supplementary Fig. 5. The calculated Young's moduli of a perfect PdTCPP-Cu (i.e. model Md00 without any significant defects) under uniaxial tensile deformation at 1 K and in vacuum is about 14 GPa, while under compression, it is only 1.3 GPa. The trajectory of two distinct processes reveals that compression to strains greater 1% causes out-of-plane deformation of PdTCPP-Cu, and the buckling surface significantly reduces resistance to deformation, resulting in one order of magnitude lower Young's modulus.

Influence of temperature, structural defects and the presence of water moisture in the elastic behavior of 2D MOF monolayer

Structural defects in 2D materials are attributed to sheets with random vacancies, line defects, and cracks mimicking grain boundaries, which significantly influence the mechanical properties[37]. Here, we investigate PdTCPP-Cu with vacancy defects distributed randomly across the monomer units, and the defect density is calculated as the ratio of missing building units to the total number of building units in a perfect layer, see model Md00 (Fig. 4b). The calculated Young's modulus in dependence on defect density under compression and tensile deformation is summarized in Fig. 5a. In tensile mode, 18.75% of defects (model Md19) cause a 70% reduction in Young's modulus, which drops further with increasing defect density. The presence of a few percent of point defects could account for the small discrepancy between the Young's modulus measured by nanoindention and the Young's modulus of PdTCPP-Cu sheets predicted by MD simulations. In the case of compression mode, the Young's modulus is hardly affected by defects, yet defects in the PdTCPP-Cu structure lead to pronounced out-of-plane deformation, even during structure relaxation (i.e. before compression starts). Unlike compression of a perfect PdTCPP-Cu (model Md00), structural defects can sometimes cause a discontinuous potential energy curve and are more likely to display step-like decreases in potential energies accompanied by a sudden increase in bending along the compression direction (Supplementary Fig. 6).

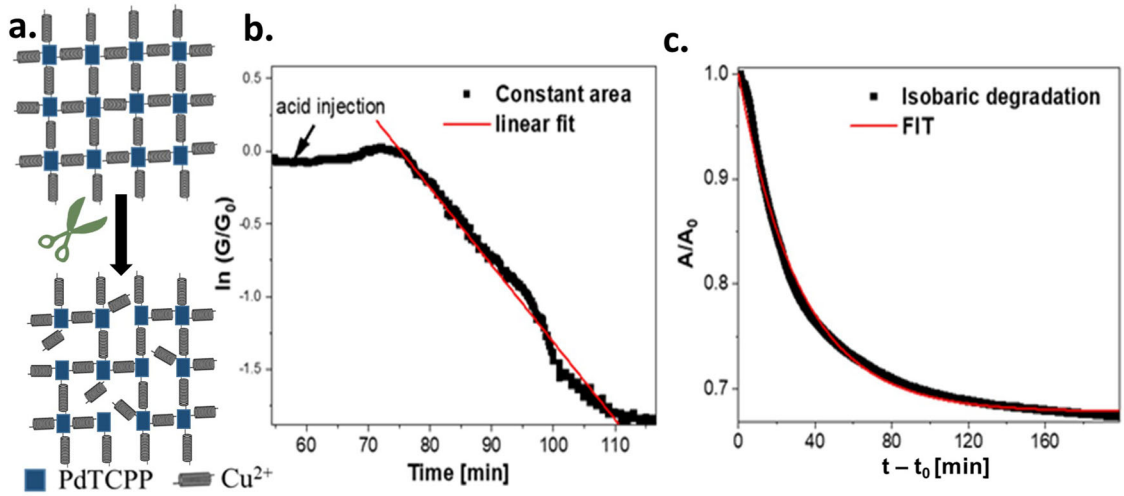

Fig. 6 Degradation of a PdTCPP-Cu monolayer. a Degradation of the representative mass spring model of the PdTCPP-Cu. **b** Experimental monolayer degradation curve of PdTCPP-Cu (reduction of shear modulus as a function of time) in acidic conditions. Degradation curves are shown from the injection point (black lines) and the corresponding fit curves are shown as red lines **c** Isobaric degradation (reduction of film area A) of PdTCPP-Cu monolayer under acidic conditions.

The Young's modulus was measured experimentally at around 300 K while the aforementioned MD simulations were performed at $T = 1$ K. Since temperature could affect the obtained Young's modulus, we ran simulations at $T = 1$ K and 300 K for comparison (Supplementary Fig. 7). Although higher temperatures cause very pronounced fluctuations in the potential energy curves, when uniaxial stretching is applied in different directions, the effect of temperature on Young's modulus on a perfect PdTCPP-Cu is very limited. However, as the density of defects increases, the pronounced fluctuations in potential energy make the calculation of Young's modulus unreliable at 300 K. As a result, only the tensile Young's modulus was investigated at that temperature.

The presence of water (moisture) could significantly impact the elastic behavior as we can see the substantial difference in Young's modulus[38,39] of PdTCPP-Cu obtained from AFM nanoindentation and in situ interfacial rheology approach. To quantify the effect of the water phase in the evaluation of the Young's modulus, finite-sized PdTCPP-Cu (model Md00) was placed on top of a well-equilibrated water layer, and the corresponding simulations were performed at 300 K in *NVT* ensemble (Supplementary Figs. 8 and 9) to determine the Young's modulus for uniaxial tensile deformation. Partial charges were introduced to better reflect the influence of water on the 2D MOF. When comparing the Young's modulus with water (Fig. 5b) and without (Supplementary Fig. 10) at 300 K and with partial charges, the Young's modulus is about 4 times lower in the presence of water. Altogether, the presence of moisture and the difference between tensile and compression deformation behavior can account for the different Young's moduli measured by nanoindentation and the Langmuir technique, with point defects being much more relevant for the former than the latter. While the Young's modulus of the 2D MOF in compression seems small in comparison to tensile deformation, it is still in the range of rather strong tissues such as muscles and tendons.

Degradation of monolayer 2D MOF

The Langmuir monolayer degradation technique has been widely used as a versatile tool to study the degradation of polymers[40,41]. By combining isobaric area reduction with interfacial rheology, it enables to study the degradation of monolayer PdTCPP-Cu synthesized at the air-water interface. By comparing to mechanistic models, such an approach can provide an understanding of laws describing the degradation of 2D materials.

To study the PdTCPP-Cu degradation, the monolayer was compressed to the degradation surface pressure (i.e. maximum compressibility modulus) of $\pi = 5$ mN m^{-1}, then the pH of the subphase was adjusted to 2 by the addition of 5 mL of 0.3 M hydrochloric acid. Given the simple tetragonal symmetry of the 2D MOF material, we hypothesize that its mechanical moduli can be described by a lattice spring model. In these models, the mechanical moduli are proportional to the number density and spring constant of linear springs per unit volume (3D), or unit area (A) in 2D[42].

$$G \sim \frac{N_{\mathrm{spring}}}{A} \tag{4}$$

$$\frac{G(t)}{G_0} = \frac{N_{\mathrm{spring}}(t)}{N_{\mathrm{spring},0}} \frac{A(t)}{A_0} \tag{5}$$

In the square lattice representation (Fig. 6a), the springs run through the coordinative copper-carboxylate bonds, and the cleavage of one bond removes a spring. To assess the evolution of the storage modulus, the network was degraded under isochoric conditions (no external compression, $A = \mathrm{const.}$), which represents the conditions a 2D MOF would experience in most real world situations. After a certain induction period required to lower and equilibrate the pH, the protons responsible for bond cleavage are available in large excess, meaning that the number of network springs decreases in a first order reaction.

$$\frac{N_{\mathrm{spring}}(t)}{N_{\mathrm{spring},0}} = e^{-kt} \tag{6}$$

$$\frac{G(t)}{G_0} = e^{-kt} \tag{7}$$

$$\ln\left(\frac{G(t)}{G_0}\right) = -kt \tag{8}$$

As can be seen in Fig. 6b, the shear modulus exhibits the predicted exponential decrease after a certain induction period. Noteworthy, the modulus shows a slight increase during that initial period. Here, we hypothesize that while the pH drops, it runs through a window where the coordinative bonds are forming reversibly, thereby enabling growth of the crystalline domains[43], resulting in fewer porphyrins in non-ideal bonding situations and

a transient increase of the areal number density of springs. When the pH drops further, bond cleavage becomes irreversible and the exponential decrease of the shear modulus sets in.

To describe the mass loss of such a 2D system, the kinetics of the bond scission need to be combined with the connectivity of the subunits. According to the first order kinetics assumed above, the probability that a bond is cut is given by:

$$\alpha = \frac{N_{\mathrm{bond},0} - N_{\mathrm{bond}}(t)}{N_{\mathrm{bond},0}} = 1 - \frac{N_{\mathrm{bond}}(t)}{N_{\mathrm{bond},0}} = 1 - e^{-kt} \quad (9)$$

If the layer consisted of an ideal network where each subunit is connected to n neighbors, removing a subunit requires to cut all n bonds to its next neighbors. Then,

$$\Delta A = A_{\mathrm{subunit}} * \alpha^n \quad (10)$$

In the real world situation, there is certainly a not insignificant fraction of molecules with a lower count of connections, e.g., at grain boundaries, point defects etc. Then,

$$\Delta A = A_{\mathrm{subunit}} * \sum_{i=1}^{n} X_i \alpha^n \quad (11)$$

where X_i is the fraction of subunits connected via i bonds and $\sum_i X_i = 1$. For the specific system PdTCPP where $n = 4$, we also observe that the porphyrins are not being dissolved when the coordinative bonds are broken and the carboxylate groups are protonated. Instead, they change their orientation from flat-on to face-on. Then, it follows that:

$$\frac{A(t)}{A_0} = \frac{A_0 - \Delta A}{A_0} = 1 - \frac{A_{\mathrm{flat}} - A_{\mathrm{Edge}}}{A_{\mathrm{flat}}} * [X_4\alpha^4 + X_3\alpha^3 + X_2\alpha^2 + X_1\alpha] \quad (12)$$

A fit of the isobaric degradation curve using the equation deduced above shows a good agreement (Fig. 6c). The resulting ratio of $\frac{A_{\mathrm{Edge}}}{A_{\mathrm{flat}}} \sim 0.68$ seems reasonable, however, the best agreement between experiment and model is obtained when $X_1 = 1$. Without detailed knowledge about the grain size distribution and the exact mechanism of the flat-on to face-on transition, it is not possible to draw a final verdict on the missing contribution from the higher order terms. Nevertheless, it is possible to imagine a packing situation where the porphyrins are in nearly edge on configuration and still bound to their nearest neighbors with three coordinative bonds, so it might be sufficient to cut only one bond to induce the change in orientation resulting in the destruction of the 2D network.

METHODS

5,10,15,20-tetrakis(4-carboxyphenyl)-porphyrinato palladium(II) (PdTCPP) was purchased from Porphyrin Laboratories GmbH, Scharbeutz, Germany. $Cu(NO_3)_2{\bullet}3H_2O$ (99.9%) and 37 wt% hydrochloric acid (HCl) were purchased from Merck, Darmstadt, Germany. Pure grades of chloroform and methanol were purchased from Merck, Darmstadt, Germany. All chemicals were used as received without further treatment. The circular mesh TEM Grids for AFM nanoindentation measurement was purchased from Science Services GmbH, München, Germany.

Synthesis of PdTCPP-Cu monolayer

The procedure to synthesize the PdTCPP-Cu film was adapted from the previously reported methods[17,28]. A PTFE "medium area" Langmuir trough (Kibron, Helsinki, Finland) with a surface area of $A = 280$ cm^2 was filled with a $Cu(NO_3)_2{\bullet}3H_2O$ (1 mM) aqueous solution as a subphase. Before filling the subphase, the trough was carefully cleaned using ethanol, acetone and water. Then, 80 µL of the 0.18 mM PdTCPP solution in chloroform/methanol solution (3:1, v/v) was spread onto the $Cu(NO_3)_2$ subphase with a microsyringe. π-MMA isotherm measurements were performed with a KSV medium area trough system by using a continuous compression speed for two barriers of 3 mm/min. The 2D array of PdTCPP-Cu at a surface pressure of 5 mN m^{-1} was transferred onto the substrate by the horizontal dipping method at room temperature. For the control experiment, 80 µL of the same PdTCPP solution was spread onto a pure water subphase. All experiments were carried out at room temperature.

Degradation of PdTCPP-Cu monolayer

Degradation experiments were carried out in a "medium area" Langmuir trough (Kibron, Helsinki, Finland) with a surface area of $A = 280$ cm^2. Firstly, the Langmuir trough was filled with a $Cu(NO_3)_2{\bullet}3H_2O$ (1 mM) aqueous solution as a subphase. Then, 80 µL of the 0.18 mM PdTCPP solution in chloroform/methanol solution (3:1, v/v) was spread onto the $Cu(NO_3)_2$ subphase with a microsyringe. To study the PdTCPP-Cu degradation, the monolayer was compressed and held at a surface pressure of 5 mN/m on a Milli-Q water subphase (pH = 6). After 200 min, the pH of the subphase was adjusted to 2 by injection of 5 mL of 0.3 M HCl into the subphase with $V = 170$ mL. All experiments were carried out at room temperature.

Interfacial rheology

Rheology was carried out with a bicone-geometry on an MCR 502 Rheometer (Anton-Paar, Graz, Austria). The bicone had a radius of $r = 25.5$ mm and was immersed in a medium sized Langmuir trough. The angle of the tip of the bicone was 166.8°. The bi-conical bob disk can be rotated or oscillated and was connected to a motor, which can detect torque τ, displacement and rotational angle. The measurements were carried out under a circular slit geometry, with a custom made ring of diameter 8 cm around the bicone. The circular ring has two openings with a width of ~2 cm, which allow the film to pass into the slit between the ring and the bicone. After the Langmuir trough was filled with sub-phase of 1 mM $Cu(NO_3)_2$ or pure water, the bicone was positioned at the interface and 80 µL of PdTCPP was spread at the edge circular ring. For the oscillatory experiments, the rotational angle was oscillated with the given amplitude and frequency. A maximum shear stress $\tau' = 1\%$ and frequency $\nu = 1$ Hz were used. The interfacial shear and loss moduli were calculated using the algorithm provided with RheoCompass software package. All experiments were carried out at room temperature.

Atomic force microscopy

Surface topography measurements and local mechanical analysis of the PdTCPP films were performed by AC-mode scanning and nanoindentation using an atomic force microscope (MFP-3D, Asylum Research, Santa Barbara, USA). AC-mode scanning was performed with OMCL-AC200TS-R3 silicon cantilevers (Olympus, Tokyo, Japan) at a scan rate of 0.5 Hz. The thickness of the PdTCPP-Cu film was determined after the film has been transferred to Si/300 nm SiO_2 substrate. A piece of mica was placed at the center of the substrate followed by horizontal transfer of PdTCPP-Cu film onto the substrate. Afterwards, the placed mica was removed, showing clear edges between the substrate and the film. The border between filled and bare substrate areas was imaged by AFM in air, and the corresponding height differences equated to the layer thickness. The analysis was carried out by averaging the height profiles along the step between substrate and film with a window width of 20 µm using the AFM surface analysis software MountainsSPIP (Digital Surf, Besançon, France). The software was also used to determine 3D areal surface texture parameter for a 40×20 µm^2 area on substrate and on the attached PdTCPP-Cu film. For the root mean square height of the surface, values of Sq =

Table 1. Number of atoms in PdTCPP-Cu 2D model systems Mdxx of different degree of defects.

	Md00	Md06	Md12	Md19	With water
$N_{atomMOF}$	1392	1396	1323	1180	1554
$N_{atomwater}$	0	0	0	0	24000

Since the defect density in our simulation is defined as the number of missing building blocks divided by the number of building blocks in a perfect 2D MOF, after the deletion of building blocks, copper paddlewheel or PdTCPP, hydrogen atoms will be added to the system, so the number of atoms in Md06 is even greater than the Md00 system. In addition, the 2D MOF in system with water is of finite size so, additional atoms were added to the cropped structure to maintain stability and ensure charge neutrality.

0.55 nm (substrate) and Sq = 0.91 nm (film) were obtained. The respective Sa (arithmetical mean height of the surface) parameters are Sa = 0.40 nm (substrate) and Sa = 0.62 nm (film).

The PdTCPP-Cu film was transferred on the circular TEM grid for the AFM based nanoindentation experiment. No additional treatment was carried out and the sheets adhered well to the circular holes which are important for the nanoindentation experiments. Finally, the TEM grid was fixed on a silicon chip using Kapton tape which resulted in good stability of the grid as observed by AFM imaging. Nanoindentation measurements were performed with cantilevers (OMCL-AC200-TS-R3) having a spring constant of 6.7 $N{\cdot}m^{-1}$.

Polarized optical microscopy

Polarized optical microscopy was performed at Zeiss Axio Imager A1m microscope (Carl Zeiss, Jena, Germany) equipped with crossed polarizers where a 40× magnification objective (Zeiss A-plan) was used.

Simulation methodologies

To investigate the Young's modulus of 2D MOF PdTCPP-Cu, a periodic supercell of 4x4x1 in *a*, *b*, and *c* dimensions were generated. Simulations were conducted with LAMMPS package version September 2021[44]. UFF4MOF force field[45,46] was adopted to optimize the 2D MOF to their minimum energy structure and also to reproduce Young's modulus property of PdTCPP-Cu. UFF4MOF benefits from its expansive coverage of periodic table including transition metal ions. Research has also shown that it can accurately reproduce bulk modulus of varies types of MOFs[47–49]. No partial charges were assigned along with UFF4MOF force field, due to the introduction of partial charges could result in worse agreements with experimental observations[47–49].

Periodic boundary conditions applies to *x* and *y*, while *z* dimension is non-periodic and fixed to prevent the interactions between MOFs in different periodic images along *z*. To evaluate the Young's modulus, the PdTCPP-Cu 2D MOF is stretched or compressed in a selected direction, unless otherwise specified, a maximum strain ε of 4% was considered by default. The *z* dimension is fixed, while the external pressure in the one remaining direction is kept around zero. The tensile or compression rate $\dot{\varepsilon}$ were tested and does not affect the simulation results, a value of $1{\times}10^{-8}$/fs was used for both tensile and compression runs throughout this work. The number of atoms and the composition of MOF and water in each case are summarized in Table 1.

Simulations were performed with time step 1 fs for initial *NVT* and *NPT* relaxations, and time step 0.5 fs were adopted for tensile and compression runs. Prior to tensile and compression runs, the atomistic models were relaxed using conjugation gradient algorithm. In addition, a self-consistent cycle was used where each cycle consisting of cell volume relaxation followed by atomic position relaxation[47]. These simulations were performed until energy difference between each cycle is less than 1×10^{-6} kcal mol^{-1}, or the maximum 100 iteration cycles was reached.

To calculate the Young's modulus *E*, uniaxial tensile and compression runs were performed in *NPT* ensemble using Nose-Hoover thermostat and barostat. The relaxation time of thermostat and barostat were 100 times and 1000 times the value of time step adopted in simulation. Van der Waals interaction cutoff distance was set to 12.5 Å, with mix arithmetic mixing rule adopted. Simulation were performed at $T = 1$ K, and $P = 0$ bar, as 1 Kelvin temperature provides kinetic energy, which allows relaxation of the molecular structure under stress[50].

The Young's modulus could be extracted from the stress–strain curve (13)

$$\sigma_x = \varepsilon_x + C_{xx}\varepsilon_x^2 \tag{13}$$

where E_x is Young's modulus in the selected direction, σ_x is the tensile or compression stress applied in the selected direction. ε_x is the resulting strain in the selected direction and C_{xx} is the second order elastic constant in the same direction. ε_x is the resulting deformation divided by the initial length

$$\varepsilon_x = (l_x - l_{x,0})/l_{x,0} \tag{14}$$

Alternatively, the Young's modulus can be calculated from the second derivative of potential energy while deformation with respective to strain[50]

$$E_{pot} = k_x \times \varepsilon_x^2 + b \times \varepsilon_x \tag{15}$$

$$E_x = 2k_x/V_0 \tag{16}$$

As shown by (15), E_{pot} is the potential energy of the system under deformation, k_x and *b* are fitting parameters of the quadratic function. V_0 is the initial volume of the 2D MOF layer, which taking into the account the layer thickness of 6 Å and initial optimized *x* and *y* dimensions. In order to make the volume calculation more accurate for 2D MOF layer with defects, the *rolling probe volume* method was used[51]. The radius of the probe was chosen so that the rolling probe volume is consistent with the volume of the perfect 2D MOF, calculated as length*width*thickness.

The Young's modulus obtained from simulations is the average of the Young's moduli E_x and E_y in *x* and *y* directions. The initial structures of the periodic 2D MOFs simulated are summarized in Fig. 4. Where the optimized unit cell of (*a*) has basal plane dimension $a = b = 16.65$ Å, which is quite consistent with the experimental XRD value of 16.6 Å[17].

To prevent water molecules from running out of the simulation box, two reflective walls were placed on the top and bottom along the *z*-direction. In addition, the *openbabel* tool[52] was used to generate partial charge following the extended charge equilibration scheme[53] (EQeq) to better describe the interaction between the water and the PdTCPP-Cu monoalyer. The Young's modulus obtained at 300 K with EQeq charge is around 4 GPa which is lower than Young's modulus without a partial charge obtained at 1 K. In order to allow for sufficient relaxation of PdTCPP-Cu on water, a stepwise tensile deformation strategy was adopted. At the same time, only the PdTCPP-Cu on the water surface was stretched and kept at a certain distance each cycle. In each stepwise deformation, the PdTCPP-Cu was stretched in increments of 0.5% of their unit cell length, and we repeated this process for 20 cycles until the 10% maximum strain was reached. After each tensile deformation, a 20000-step relaxation of the *NVT* atomic positions was performed in LAMMPS while maintaining a specific strain on the PdTCPP-Cu along the selected direction. These were achieved by the *smd* method of LAMMPS by applying additional forces on selected groups of atoms. The well-relaxed system, the system with PdTCPP-Cu stretched by 10% are demonstrated in

Supplementary Fig. 8, and the stepwise tensile scheme and the stress-strain curve along deformation are summarized in Supplementary Fig. 9 and Fig. 5b. Unlike the pure 2D MOF without water, the potential fluctuation of the MOF on the water layer is too large to extract information from it. The Young's modulus of the 2D MOF on the water layer is calculated from the slope of the stress-strain curve.

DATA AVAILABILITY

The datasets generated during the current study are available online under https://doi.org/10.5281/zenodo.7782736.

CODE AVAILABILITY

Programs are available from the corresponding author on reasonable request.

Received: 23 September 2022; Accepted: 10 March 2023;
Published online: 01 April 2023

REFERENCES

1. Das, S., Gulotty, R., Sumant, A. V. & Roelofs, A. All Two-Dimensional, Flexible, Transparent, and Thinnest Thin Film Transistor. *Nano Lett.* **14**, 2861–2866 (2014).
2. Bae, S.-H. et al. Graphene-based transparent strain sensor. *Carbon* **51**, 236–242 (2013).
3. Zhu, S.-E., Krishna Ghatkesar, M., Zhang, C. & Janssen, G. C. A. M. Graphene based piezoresistive pressure sensor. *Appl. Phys. Lett.* **102**, 161904 (2013).
4. Wu, W. et al. Piezoelectricity of single-atomic-layer MoS 2 for energy conversion and piezotronics. *Nature* **514**, 470–474 (2014).
5. Eichler, A. et al. Nonlinear damping in mechanical resonators made from carbon nanotubes and graphene. *Nat. Nanotech.* **6**, 339–342 (2011).
6. Keskin, S. & Kızılel, S. Biomedical Applications of Metal Organic Frameworks. *Ind. Eng. Chem. Res.* **50**, 1799–1812 (2011).
7. Zhan, H., Guo, D. & Xie, G. Two-dimensional layered materials: from mechanical and coupling properties towards applications in electronics. *Nanoscale* **11**, 13181–13212 (2019).
8. Liu, J. & Wöll, C. Surface-supported metal–organic framework thin films: fabrication methods, applications, and challenges. *Chem. Soc. Rev.* **46**, 5730–5770 (2017).
9. Allendorf, M. D. et al. Stress-Induced Chemical Detection Using Flexible Metal−Organic Frameworks. *J. Am. Chem. Soc.* **130**, 14404–14405 (2008).
10. Venkatasubramanian, A. et al. MOF @ MEMS: Design optimization for high sensitivity chemical detection. *Sensors Actuators B: Chem.* **168**, 256–262 (2012).
11. Freund, P. et al. The force of MOFs: the potential of switchable metal–organic frameworks as solvent stimulated actuators. *Chem. Commun.* **56**, 7411–7414 (2020).
12. Sun, Y., Hu, Z., Zhao, D. & Zeng, K. Probing nanoscale functionalities of metal–organic framework nanocrystals. *Nanoscale* **9**, 12163–12169 (2017).
13. Stock, N. & Biswas, S. Synthesis of Metal-Organic Frameworks (MOFs): Routes to Various MOF Topologies, Morphologies, and Composites. *Chem. Rev.* **112**, 933–969 (2012).
14. Dong, R., Zhang, T. & Feng, X. Interface-Assisted Synthesis of 2D Materials: Trend and Challenges. *Chem. Rev.* **118**, 6189–6235 (2018).
15. Sahabudeen, H., Dong, R. & Feng, X. Interfacial Synthesis of Structurally Defined Organic Two-dimensional Materials: Progress and Perspectives. *CHIMIA International Journal for Chemistry* **73**, 480–486 (2019).
16. Wang, L., Sahabudeen, H., Zhang, T. & Dong, R. Liquid-interface-assisted synthesis of covalent-organic and metal-organic two-dimensional crystalline polymers. *npj 2D Mater Appl.* **2**, 1–7 (2018).
17. Makiura, R. & Konovalov, O. Interfacial growth of large-area single-layer metal-organic framework nanosheets. *Sci. Rep.* **3**, 2506 (2013).
18. Xu, G., Yamada, T., Otsubo, K., Sakaida, S. & Kitagawa, H. Facile "Modular Assembly" for Fast Construction of a Highly Oriented Crystalline MOF Nanofilm. *J. Am. Chem. Soc.* **134**, 16524–16527 (2012).
19. Braslau, A. et al. Surface Roughness of Water Measured by X-Ray Reflectivity. *Phys. Rev. Lett.* **54**, 114–117 (1985).
20. Servalli, M. & Schlüter, A. D. Synthetic Two-Dimensional Polymers. *Ann. Rev. Mater. Res.* **47**, 361–389 (2017).
21. Sakaida, S. et al. Crystalline coordination framework endowed with dynamic gate-opening behaviour by being downsized to a thin film. *Nat. Chem* **8**, 377–383 (2016).
22. Zheng, Z. et al. Square-Micrometer-Sized, Free-Standing Organometallic Sheets and Their Square-Centimeter-Sized Multilayers on Solid Substrates. *Macromol. Rapid Commun.* **34**, 1670–1680 (2013).
23. Hermosa, C. et al. Mechanical and optical properties of ultralarge flakes of a metal–organic framework with molecular thickness. *Chem. Sci.* **6**, 2553–2558 (2015).
24. Zeng, Z., Flyagina, I. S. & Tan, J.-C. Nanomechanical behavior and interfacial deformation beyond the elastic limit in 2D metal–organic framework nanosheets. *Nanoscale Adv.* **2**, 5181–5191 (2020).
25. Sahabudeen, H. et al. Wafer-sized multifunctional polyimine-based two-dimensional conjugated polymers with high mechanical stiffness. *Nat. Commun.* **7**, 13461 (2016).
26. Song, Z., Artyukhov, V. I., Wu, J., Yakobson, B. I. & Xu, Z. Defect-Detriment to Graphene Strength Is Concealed by Local Probe: The Topological and Geometrical Effects. *ACS Nano* **9**, 401–408 (2015).
27. Cao, K. et al. Elastic straining of free-standing monolayer graphene. *Nat. Commun.* **11**, 284 (2020).
28. Motoyama, S., Makiura, R., Sakata, O. & Kitagawa, H. Highly Crystalline Nanofilm by Layering of Porphyrin Metal−Organic Framework Sheets. *J. Am. Chem. Soc.* **133**, 5640–5643 (2011).
29. Lu, W., Knobler, C. M., Bruinsma, R. F., Twardos, M. & Dennin, M. Folding Langmuir monolayers. *Phys. Rev. Lett* **89**, 146107 (2002).
30. Thorpe, M. F. & Jasiuk, I. New results in the theory of elasticity for two-dimensional composites. *Proc. Royal Soc. London. Series A: Mathe. Phys. Sci.* **438**, 531–544 (1992).
31. Makiura, R. et al. Surface nano-architecture of a metal–organic framework. *Nat. Mater* **9**, 565–571 (2010).
32. Cicuta, P. & Terentjev, E. M. Viscoelasticity of a protein monolayer from anisotropicsurface pressure measurements. *Eur. Phys. J. E* **16**, 147–158 (2005).
33. Harrison, K. L., Biedermann, L. B. & Zavadil, K. R. Mechanical Properties of Water-Assembled Graphene Oxide Langmuir Monolayers: Guiding Controlled Transfer. *Langmuir* **31**, 9825–9832 (2015).
34. Bouakaz, B. S., Habi, A., Grohens, Y. & Pillin, I. Effect of combinations of nanofillers on rheology-structure relations in biodegradable poly(ε-caprolactone) nanocomposites. *Appl. Clay Sci.* **161**, 35–47 (2018).
35. Davies, J. T. *Interfacial Phenomena*. (Elsevier, 2012).
36. Turchanin, A. et al. One Nanometer Thin Carbon Nanosheets with Tunable Conductivity and Stiffness. *Adv. Mater.* **21**, 1233–1237 (2009).
37. Burtch, N. C., Heinen, J., Bennett, T. D., Dubbeldam, D. & Allendorf, M. D. Mechanical Properties in Metal–Organic Frameworks: Emerging Opportunities and Challenges for Device Functionality and Technological Applications. *Adv. Mater.* **30**, 1704124 (2018).
38. Bu, W. et al. The computational study of moisture effect on mechanical behavior of baghdadite matrix via molecular dynamics approach. *J. Mater. Res. Technol.* **15**, 2828–2836 (2021).
39. Sahputra, I. H., Alexiadis, A. & Adams, M. J. Effects of Moisture on the Mechanical Properties of Microcrystalline Cellulose and the Mobility of the Water Molecules as Studied by the Hybrid Molecular Mechanics–Molecular Dynamics Simulation Method. *J. Polymer Sci. Part B: Polymer Phys.* **57**, 454–464 (2019).
40. Schöne, A.-C., Roch, T., Schulz, B. & Lendlein, A. Evaluating polymeric biomaterial–environment interfaces by Langmuir monolayer techniques. *J. Royal Soc. Interface* **14**, 20161028 (2017).
41. Machatschek, R., Schulz, B. & Lendlein, A. Langmuir Monolayers as Tools to Study Biodegradable Polymer Implant Materials. *Macromol. Rapid Commun.* **40**, 1800611 (2019).
42. Ostoja-Starzewski, M. Lattice models in micromechanics. *Appl. Mech. Rev.* **55**, 35–60 (2002).
43. Qi, H. et al. Near–atomic-scale observation of grain boundaries in a layer-stacked two-dimensional polymer. *Sci. Adv.* **6**, eabb5976 (2020).
44. Thompson, A. P. et al. LAMMPS - a flexible simulation tool for particle-based materials modeling at the atomic, meso, and continuum scales. *Comp. Phys. Commun.* **271**, 108171 (2022).
45. Addicoat, M. A., Vankova, N., Akter, I. F. & Heine, T. Extension of the Universal Force Field to Metal–Organic Frameworks. *J. Chem. Theory Comput.* **10**, 880–891 (2014).
46. Coupry, D. E., Addicoat, M. A. & Heine, T. Extension of the Universal Force Field for Metal–Organic Frameworks. *J. Chem. Theory Comput.* **12**, 5215–5225 (2016).
47. Boyd, P. G., Moosavi, S. M., Witman, M. & Smit, B. Force-Field Prediction of Materials Properties in Metal-Organic Frameworks. *J. Phys. Chem. Lett.* **8**, 357–363 (2017).
48. Madsen, R. S. K. et al. Mixed metal node effect in zeolitic imidazolate frameworks. *RSC Adv.* **12**, 10815–10824 (2022).
49. Vanduyfhuys, L. et al. Extension of the QuickFF force field protocol for an improved accuracy of structural, vibrational, mechanical and thermal properties of metal–organic frameworks. *J. Comput. Chem.* **39**, 999–1011 (2018).

50. Li, H. & Brédas, J.-L. Impact of Structural Defects on the Elastic Properties of Two-Dimensional Covalent Organic Frameworks (2D COFs) under Tensile Stress. *Chem. Mater.* **33**, 4529–4540 (2021).
51. Voss, N. R. & Gerstein, M. 3V: cavity, channel and cleft volume calculator and extractor. *Nucleic Acids Res.* **38**, W555–W562 (2010).
52. O'Boyle, N. M. et al. Open Babel: An open chemical toolbox. *J. Cheminform.* **3**, 33 (2011).
53. Wilmer, C. E., Kim, K. C. & Snurr, R. Q. An Extended Charge Equilibration Method. *J. Phys. Chem. Lett.* **3**, 2506–2511 (2012).

ACKNOWLEDGEMENTS

This work was financially supported by the Helmholtz Association through program-oriented funding.

AUTHOR CONTRIBUTIONS

H.S.: Conceptualization, Investigation, Formal analysis, Visualization, Writing – Original Draft. Q.Z.: Methodology, Investigation, Visualization, Software, Formal analysis, Writing – Original Draft. Y.L.: Investigation, Formal analysis, Writing – Original Draft. M.H.: Methodology, Writing - Original Draft. R.M.: Conceptualization, Project Administration, Methodology, Formal analysis, Visualization, Writing – Original Draft.

FUNDING

Open Access funding enabled and organized by Projekt DEAL.

COMPETING INTERESTS

The authors declare no competing interests.

ADDITIONAL INFORMATION

Supplementary information The online version contains supplementary material available at https://doi.org/10.1038/s41699-023-00391-3.

Correspondence and requests for materials should be addressed to Rainhard Machatschek.

Reprints and permission information is available at http://www.nature.com/reprints

Publisher's note Springer Nature remains neutral with regard to jurisdictional claims in published maps and institutional affiliations.